Solid Freeform Fabrication 2017: Proceedings of the 28th Annual International Solid Freeform Fabrication Symposium – An Additive Manufacturing Conference
Reviewed Paper

Microheater Array Powder Sintering: A Novel Additive Manufacturing Process

Nicholas Holt, Austin VanHorn, Mahsa Montazeri, Wenchao Zhou
The AM[3] Lab, Department of Mechanical Engineering, University of Arkansas at Fayetteville
Fayetteville, AR, United States of America; email: zhouw@uark.edu

ABSTRACT

One of the most versatile additive manufacturing (AM) processes is selective laser sintering (SLS), which scans a powder bed with a laser beam to fuse powder particles layer by layer to build 3D objects for prototypes and end products with a wide range of materials. However, it suffers from slow printing speed due to the pointwise scanning and high energy consumption due to the requirement of a high-power laser. In this paper, we propose a novel method of additive manufacturing which replaces the laser beam with an array of microheaters as an energy source to sinter powder particles. This method, referred to as Microheater Array Powder Sintering (MAPS), has the potential to significantly increase the printing speed by layer-wise sintering and reduce the power consumption due to the lower power requirements of the microheater array. This paper is to provide a proof-of-concept for this proposed new method. First, a thin-film microheater is designed and simulated with an experimentally validated numerical model to demonstrate that it can be used as an alternative energy source to sinter powder particles by reaching a target temperature of 600°C within milliseconds at a power consumption of 1.2 Watts. The numerical model is used to simulate the MAPS process by placing the heater in close proximity to the powder particles. Simulation results show that heat can be effectively transferred over an air gap to raise the temperature of the powder particles to their sintering temperature. Different process parameters (e.g., air gap, material properties, time, printing resolution, etc.) are discussed. An experimental MAPS system is then implemented to provide a proof-of-concept with the designed microheater and a custom air gap control apparatus. A straight line is successfully printed on thermal paper using the experimental MAPS system, which suggests the proposed MAPS process is feasible.

Key words: Additive manufacturing, MAPS, MEMS, microheaters, printed electronics, powder bed processes

1. INTRODUCTION

1.1. Background and Motivation

Additive manufacturing (AM) is becoming increasingly popular due to its ability to form almost arbitrary shapes, which offers a wide range of customizable products as well as a great method of prototyping. Most additive processes are burdened by their slow printing speed, which has prevented AM from becoming a viable alternative to traditional manufacturing. The motivation for this research is to develop a method of printing which has the potential to significantly exceed the performance of industry standards in terms of printing speed while minimizing power consumption.

1.2. Literature Review

Selective laser sintering (SLS), developed at the University of Texas at Austin, was among the first commercialized AM processes [1]. It uses a laser beam as the energy source to selectively induce fusion between powder particles layer by layer to build 3D structures. Originally developed to produce plastic prototypes (e.g., Nylon) using a point-wise laser scanning technique, SLS was

subsequently extended to process metal and ceramic powders based on different sintering mechanisms [2], such as solid state sintering, chemical induced sintering, liquid phase sintering, and full melting [3-6]. Alternative energy sources have also been utilized, such as electron beam. These variants of SLS are categorized as powder bed fusion (PBF) process, which has proven to be the most flexible general approach to AM due to its capability of working with a broad range of materials (including polymers, metals, ceramics, and composites) to directly manufacture end-use products with engineering-grade properties [7]. Unlike laser beams that heat the powder when photons are absorbed by powder particles, electron beams heat powder by imparting the kinetic energy of accelerated electrons to the powder particles as utilized in the electron beam melting (EBM) process commercialized by Arcam AB (recently acquired by General Electric) [8]. Although it is more efficient to convert electrical energy into an electron beam than laser, and thus cheaper to achieve higher beam energies, the system poses a problem. The powder particles can be negatively charged by the electrons in the EBM and the repulsive forces between the negative charges can create a powder cloud due to the rapid expulsion of powder particles. This in turn repels incoming electrons, which typically require the powder bed of EBM to be very conductive and the minimum feature and powder particle size for EBM to be larger than that for SLS; this is to avoid the buildup of electron charges in the powder bed [9]. Extensive research and significant progress have been reported on understanding of the PBF processes (e.g., energy absorption by the materials, sintering kinetics, phase transformation, thermal expansion, heat transfer, wetting, etc.), and on optimizing the process parameters [5, 6, 10] to improve the accuracy and the properties of the finished parts [11-14].

However, the SLS and EBM processes suffer from slow manufacturing speed, which is primarily limited by the point-wise scanning process. Several other powder-bed processes have been developed or have been under development to address this issue, including multi-beam laser additive manufacturing (MB-LAM) [15], selective mask sintering (SMS) [16], high-speed sintering (HSS) [17], selective inhibition sintering (SIS) [18, 19], and binder jetting [20]. MB-LAM uses two or more laser beams to scan simultaneously to increase productivity, but it would be very challenging and expensive to scale up using this approach as the complexity and cost of the system increase with the number of lasers. SMS, commercialized by Sintermask GmbH, fuses an entire layer of powder in a single exposure to reduce time using an infrared lamp that projects the energy pattern of the layer through a dynamic mask, which is formed by electrostatically depositing toner on a glass plate for each layer (similar to that used in a photocopier). This method prints at a speed of 10 to 20 seconds per layer with a layer thickness of 50 to 120 μm. Due to its layer-wise manufacturing approach, it can print about four times faster than a comparable SLS system at about one third of the costs. Due to the use of relatively low-power infrared lamps, no protecting environment (e.g., with nitrogen gas) is necessary as typically required for SLS systems. One main drawback of SMS is the limit of material choices due to the use of an infrared energy source, which requires the powder materials can readily absorb infrared light (typically dark-colored materials). HSS, originally developed at Loughborough University, also uses an infrared lamp to quickly scan over an entire layer to sinter the powder particles. The sintering pattern for each layer is achieved by depositing inks that are formulated to significantly enhance the absorptivity of infrared energy of the powders in the desired region using an inkjet printhead. By processing one layer at a time, HSS can print significantly faster than comparable SLS systems at a few seconds per layer with a lower machine cost due to the elimination of the laser. SIS, originally developed at the University of Southern California, is a similar process to HSS that also uses inkjet. Unlike HSS, SIS prints ink that inhibits the sintering of the powder particles at the

outline of the desired geometry on each layer. A 3D structure can be fabricated by applying infrared radiation to each layer or bulk sintering all the layers in an oven. Although full information is not yet available, the HP's multi-jet fusion technology appears to be similar to HSS or SIS or a combination of both by ink-jetting multiple chemical agents onto the powder layer. HP claims that the multi-jet fusion process can print ~10 times faster than comparable SLS systems. Binder jetting, originally developed at the Massachusetts Institute of Technology (MIT) in the early 1990s and commercialized by ZCorp (now part of 3D Systems) and ExOne, is another similar process that uses an inkjet printhead to print binders onto a powder bed to join the powder particles together layer by layer. The printed green part (i.e., the bonded layers) needs to be post-sintered in an oven and infiltration of infiltrant materials is often needed to increase the density and the strength of the part. Although the printing speed of binder jetting is relatively fast, the post processing can take hours or even longer.

Although these processes as they are being further developed will undoubtedly provide a boost to the 3D printing industry, they have two main drawbacks. *One* is the energy source for sintering. Infrared radiation is an indirect energy source that needs to be converted into heat for sintering, which often imposes material-specific limitations and requires extra time for the powders to absorb the radiation. Bulk sintering is not energy-efficient and not accurate because it typically requires a high-temperature oven and cannot accurately control the local sintering process on the scale of the powder particles. Therefore, it is beneficial to use an energy source that can directly deliver heat patterns because heat can be absorbed by any material. Direct heat patterns have been utilized for material processing and printing before. Scanning thermal lithography [21] was developed as a maskless lithography technique that uses a scanning thermal probe to pattern photoresist with a submicron resolution. Thermal printing (direct thermal printing or thermal transfer printing), which operates at relatively low temperature (~ 300 °C), has long been used in the point-of-sale (POS) printers by applying heat patterns in a contact mode to heat-sensitive papers to print receipts [22]. Selective heat sintering (SHS) [23], which uses a commercial thermal printhead to transfer heat through an 80μm-thick protective thin-film sheet to selectively heat the powder particles. However, due to the low operation temperature of the commercial thermal printhead and the plastic protective sheet, the temperature of the powder particles can only be raised by a few degrees and the powder bed has to be preheated to just a few degrees below the sintering temperature of the powder particles, causing significant energy waste and limiting its potential (especially for high-temperature materials). *The second drawback* is the exposure timescale. Sintering typically takes place in a few milliseconds in SLS systems when laser or electron beam scan over the powder particles (~100μm) at a speed of ~100mm/s due to the high energy density of laser or electron beam (i.e., each particle get exposure for ~1 ms) [7], while it generally requires much longer exposure time (~1s) for the aforementioned processes that use infrared radiation [17, 24, 25].

1.3. Overview of this paper

To overcome these two drawbacks, we propose to use a high-temperature microheater array as the energy source to create and apply a heat pattern directly to the powder particles in a non-contact mode by placing the microheater in a close proximity to the substrate (termed as Microheater Array Powder Sintering, or MAPS), which can deliver a very high energy density in a few milliseconds for fast sintering as does laser or electron beam. In this paper, we will provide a proof-of-concept for this new printing method. In section 2, we will simulate the operation of a designed microheater for the MAPS process using an experimentally validated numerical model. Section 3 will simulate

the operation of the proposed MAPS process. Results and several critical process parameters for MAPS (e.g., air gap, material properties, time, printing resolution, etc.) are discussed in section 4. Possible improvements of the MAPS system are discussed in section 5. In section 6, we implemented an experimental MAPS system and provided a preliminary experimental proof-of-concept and demonstrated the feasibility of the proposed MAPS process. Conclusions and future work are presented in section 7.

2. Simulation of the Microheater Operation

2.1. Design of Microheater

A microheater is a tiny thin film resistor that can be fabricated at relatively low costs using MEMS fabrication techniques. Sizes of heating elements can range from ~100nm to ~100µm and can be made from heating materials such as platinum, tungsten or molybdenum. Depending on the size and application, a microheater typically operates at a kHz frequency with a power consumption of ~100mW and can achieve a heating temperature of over 1000°C [26]. A typical configuration of a microheater is shown in Figure 1.

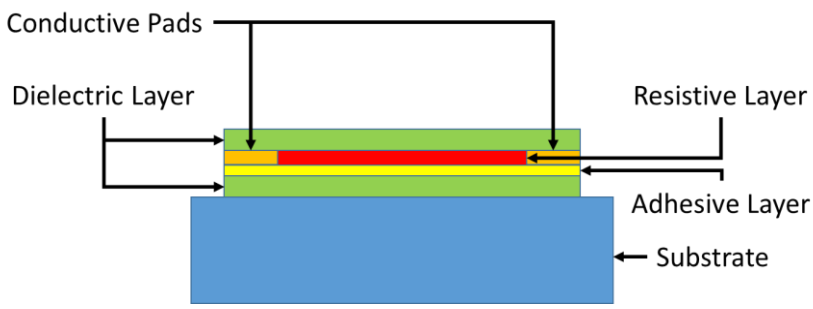

Figure 1 - Typical configuration of a microheater

For an initial proof-of-concept, it was desired to design a heater which had the following attributes for the proposed MAPS process:

1. A target temperature of 600°C;
2. A heating and cooling cycle on the timescale of ~1ms;
3. Minimal power consumption.

In this paper, an ultra-thin glass (type AF 32 eco from Schott Inc.) was used as a substrate to support the resistive filament and conductive leads; this material was chosen due to its low thermal conductivity, making it more power efficient [27], and this glass has a high transition temperature of 717°C which is higher than the desired temperature of the microheater. Titanium was chosen as the heater filament, and gold was chosen as the leads to the heater due to its high electrical conductivity and low coefficient of thermal expansion compared to other typical conductors such as silver; this will reduce stresses in the design. The material properties are as follows:

Table 1 - Properties of materials used in simulations

Summary	Titanium (Ti)	Ultra-Thin Glass	Gold (Au)
Electrical Resistivity (Ω*m) @ 20°C	1.54E-06	-	2.77E-08
Temperature Coefficient of Resistance (1/°C)	3.50E-03	-	0.0034
Thermal Expansion Coefficient (1/K)	8.60E-06	3.20E-06	1.42E-05
Thermal Conductivity (W/m*K)	21.9	1.16	3.17E+02
Specific Heat (J/kg*K)	522	820	129
Density (kg/m^3)	4507	2430	19300
Young's Modulus (Pa)	1.16E+11	7.29E+10	7.00E+10
Poisson's ratio (1)	0.321	0.208	0.44
Thickness (µm)	0.2	50	0.2
Purpose	Resistor	Substrate	Conductor

A design was desired that would reduce stress and temperature variation across the surface of the heater, so a steering-wheel design was used as shown in Figure 2. The dimensions of the heater were optimized using particle swarm method, which is described in our previous research [28].

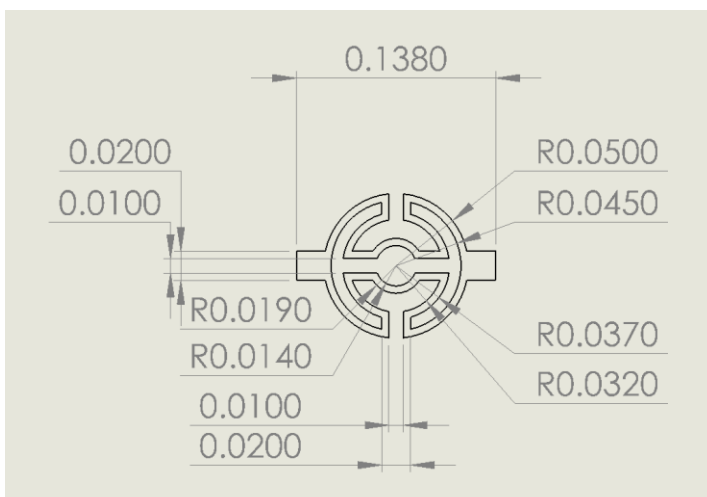

Figure 2 - Dimensions of an optimized titanium microheater (unit: mm)

2.2. Numerical Simulation

These materials and the heater configuration described above were simulated using an experimentally validated COMSOL model to verify that the design of the microheater would meet our design requirements [28]. The model was constructed with the following constraints:

1. The heater filament and leads were modeled as a thin film of 150nm;
2. The filament was placed in the center of a section of substrate 200µm square by 50µm thick;
3. The sides of the substrate were modeled as open boundaries, and heat flux from the top and bottom of the die were modeled using convective heat flux with a heat transfer coefficient of $h = 5\ W/m^2*K$ [28].
4. The initial temperature of the model was 20°C.

A power of 1.2W was applied across the leads of this model for this simulation. A boundary probe was utilized at the heater filament to capture the temperature of the microheater, and a time dependent study was used over a range of two milliseconds to observe the heater's response.

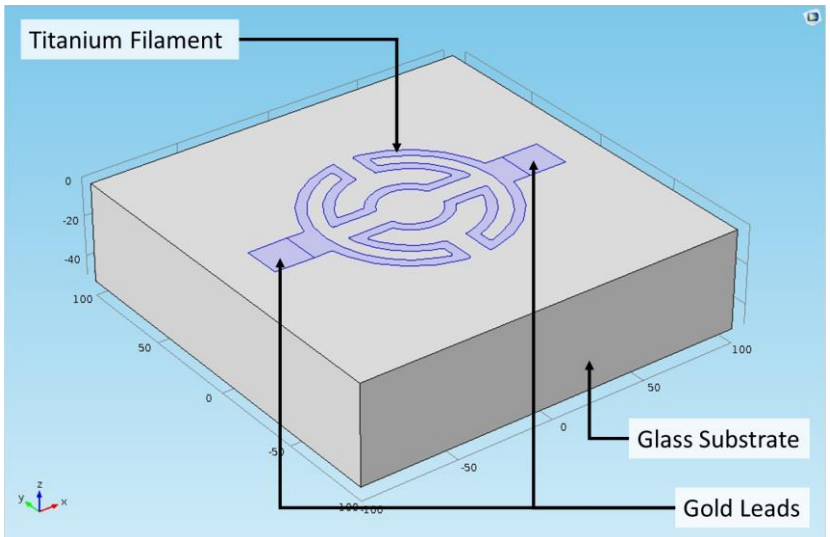

Figure 3 - COMSOL model of microheater

2.3. Simulation Results

The results of the simulation can be seen in Figure 4: with a power input of 1.2W for 1 millisecond, the heater reaches a temperature of 600°C in 1ms as set forth in the design constraints. It can also be seen that the heater cools from 600°C to 182°C in 1ms by natural cooling. This simulation showed that this design would meet our heating requirements, and in the next section we will show that this heater can be used to sinter select materials.

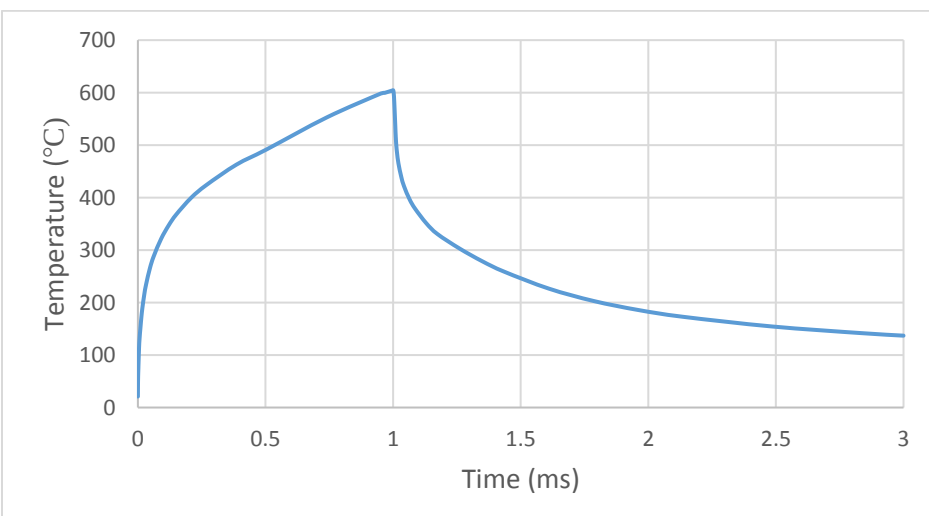

Figure 4 - Temperature ramp for the microheater at 1.2W for 1ms followed by natural cooling

3. SIMULATION OF THE MAPS SYSTEM

3.1. Description of setup

The numerical model of the microheater previously described is used again for simulating the printing system. In this study, the microheater is placed over the material being sintered which is placed on top of another glass substrate (or the printing substrate). The heater and the sintering material is separated by an air gap, modeled as a fluid; this air gap is the medium through which the heat transfer from the heater to the sintered material occurs. An overview of the setup can be seen in Figure 5.

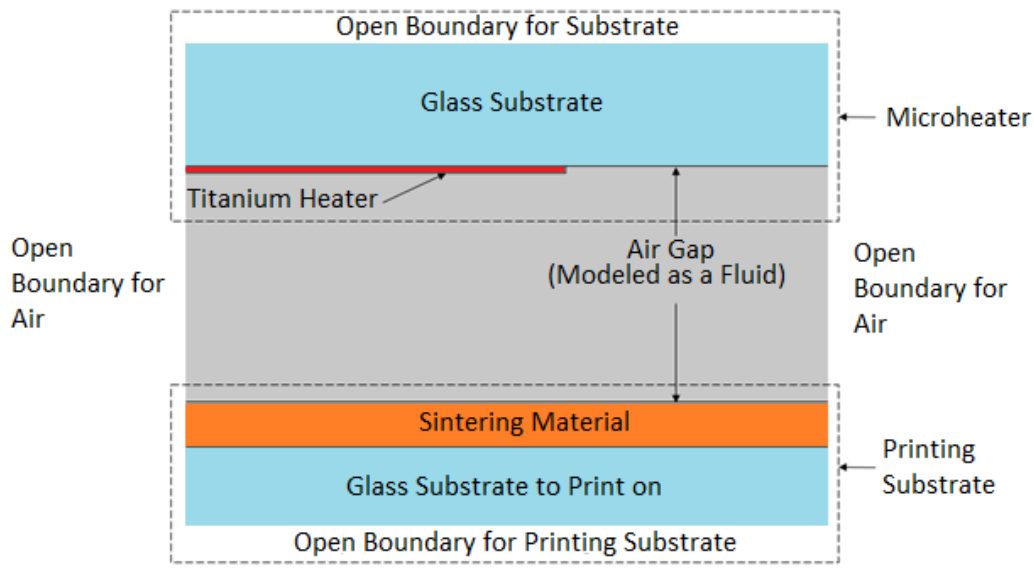

Figure 5 - Modeling setup of MAPS scenario

To simplify the numerical model, open boundaries have been used where boundaries would be continuous. The initial temperature in the simulation is 20^0 C. Material properties are the same for the microheater part of the simulation. Air has material properties that are temperature dependent, which are modeled based on known relationships [29]. The printing substrate is Pyrex 7740 glass. The additional material properties used at room temperature are in Table 2.

Table 2 - Properties of additional materials

Summary	Pyrex-7740	Air
Electrical Resistivity (Ω*m)	1.26E+06	-
Thermal Conductivity (W/m*K)	1.18	.0257 or >
Specific Heat (J/kg*K)	753.12	1.005 or >
Density (kg/m^3)	2230	1.225 or >
Temperature Coefficient of Resistance (1/K)	-	-
Young's Modulus (Pa)	1.16E+11	-
Poisson's ratio (1)	0.321	-
Thermal Expansion Coefficient (1/K)	8.60E-06	-
Function	Substrate	Conducting Medium
Thickness (μm)	550	0 to 50

3.2. Parameters of the study

For our simulations in this paper, we will use silver nanoparticles as the material to be sintered, such as the dried silver nanoparticles offered by NanoComposix [30]. NanoComposix offers this powder in various sizes, but for our study we will focus on a particle size of 50nm. The objective of this simulation is to numerically validate that the resistive heating source previously designed can provide adequate heat to elevate the temperature of the powder to sintering temperature. Temperatures will be measured at the surface of the silver nanoparticles being sintered to make this determination. Relevant parameters that will be investigated in this study include the air gap, temperature on the surface of the particle layer, and sintering resolution based on a 1ms heater ramp to 600°C.

3.2.1. Effective thermal conductivity of particles

Modeling the thermal conductivity of the powder particles is an essential aspect of accurate prediction. In these simulations, we will model the powder particles as a combination of densely populated nanoparticles and air as mentioned above. Thus, the powders can be treated as a bulk thin film material with an effective bulk thermal conductivity given by Equation 1, which has been shown to be accurate in simulations [31-34]:

$$\frac{k}{k_g} = \left(1-\sqrt{1-\varepsilon}\right)\left(1+\frac{\varepsilon k_r}{k_g}\right)+\sqrt{1+\varepsilon}\left[(1-\varphi)\left(\frac{2}{1-\frac{Bk_g}{k_s}}\left(\frac{B}{\left(1-\frac{Bk_g}{k_s}\right)^2}\left(1-\frac{k_g}{k_s}\right)\ln\left(\frac{k_s}{Bk_g}\right)-\frac{B+1}{2}-\frac{B-1}{1-\frac{Bk_g}{k_s}}\right)+\frac{k_r}{k_g}\right)+\frac{\varphi k_s}{k_g}\right] \quad (1)$$

Where:

k = effective thermal conductivity of the powder bed in W/m-K
k_g = thermal conductivity of the gas inside the pores of the powder bed, W/m-K
k_s = thermal conductivity of the skeletal solid, W/m-K
ε = porosity of the powder bed
k_r = thermal conductivity part of the powder bed owing to radiation, denoted by the Damkoler's equation below, W/m-K
φ = flattened surface fraction of particle in contact with another particle; φ = 0 when there is no contact between the particles; φ = 1 when there is complete contact between particles (i.e. fully compacted)
B = deformation parameter of the particle; for B < 1, the particle is a prolonged needle; B = 1 for spherical particles, and B > 1 is a barrel-like body

$$k_r = \xi s d_p e \sigma \left(T_b^2 + T_i^2\right)(T_b + T_i) = 4\xi s d_p e \sigma T_b^3 \quad (2)$$

Where:
ξ = the area fraction occupied by the canals for the radiation per total unit area
s = a numerical factor about 1
d_p = the diameter of the powder particle
e = emissivity
σ = Stefan-Boltzmann constant = 5.67E-8 W/m^2-K^4
T_b = temperature of the powder bed
T_i = temperature of the surrounding assumed to be near T_b

Equation 1 was used to calculate the thermal conductivity of the material being sintered. The powder in this case was silver, which has a bulk thermal conductivity of 406 W/m*K. This equation will be used to predict the bulk thermal conductivity of silver nanoparticles in air to replicate the heat transfer in the printing scenario. The thermal conductivity of the silver particles based on this equation is shown in Figure 6.

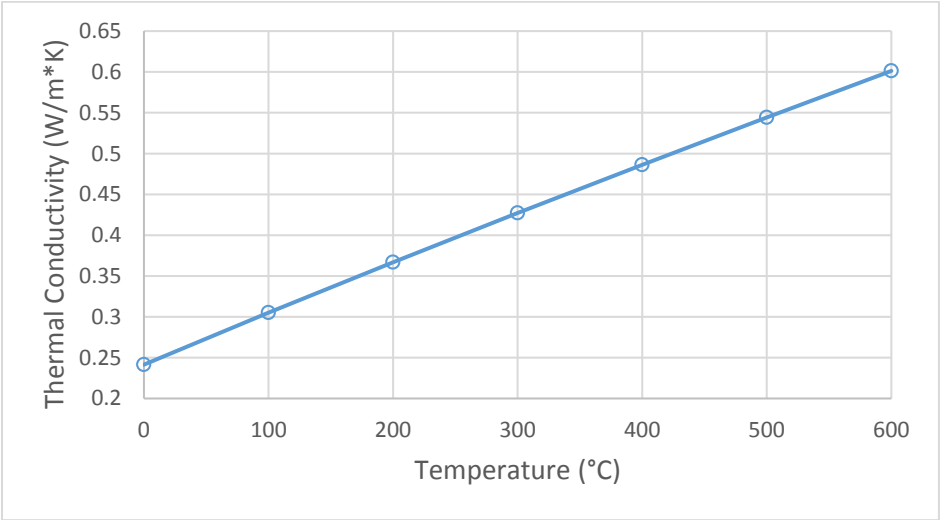

Figure 6 - Thermal conductivity of silver nanoparticles

This shows that the effective thermal conductivity of silver nanoparticles in air is significantly lower than the bulk thermal conductivity of silver. This model will be used as the effective thermal conductivity of the silver nanoparticles in the following simulations.

4. Simulation Results of The MAPS System

4.1. Power requirements

With the calculated effective thermal conductivity, a 3D simulation is performed to evaluate the sintering of the silver nanoparticles using the MAPS process and the results are illustrated in Figure 6. It is worth noting that our simulation results show it takes a power input of 2.1W for the microheater to reach 600°C in 1 millisecond with the silver nanoparticles underneath in contrast to 1.2W shown previously shown in **Error! Reference source not found.**; this is because the sintering materials conducts heat away. This suggests it is possible to determine the sintering state of the materials (the effective thermal conductivity will change as the materials are being sintered) by monitoring the temperature change in the microheater in the future. Because the microheater can be used as a resistive temperature sensor, the proposed MAPS process can therefore provide an inherent in-situ monitoring mechanism of the sintering process. Based on our preliminary simulations, it was shown 1 millisecond was insufficient to heat the silver nanoparticles to an acceptable sintering temperature; we have chosen to ramp up the heater temperature to 600°C in 1ms and then maintain it for 14ms for the silver nanoparticles to achieve a sufficiently high sintering temperature.

4.2. Effects of air gap

Using these parameters, the next goal is to see how the temperature on the surface of the nanoparticles will be affected by varying the air gap from 1µm to 30µm. These results are provided in Figure 7.

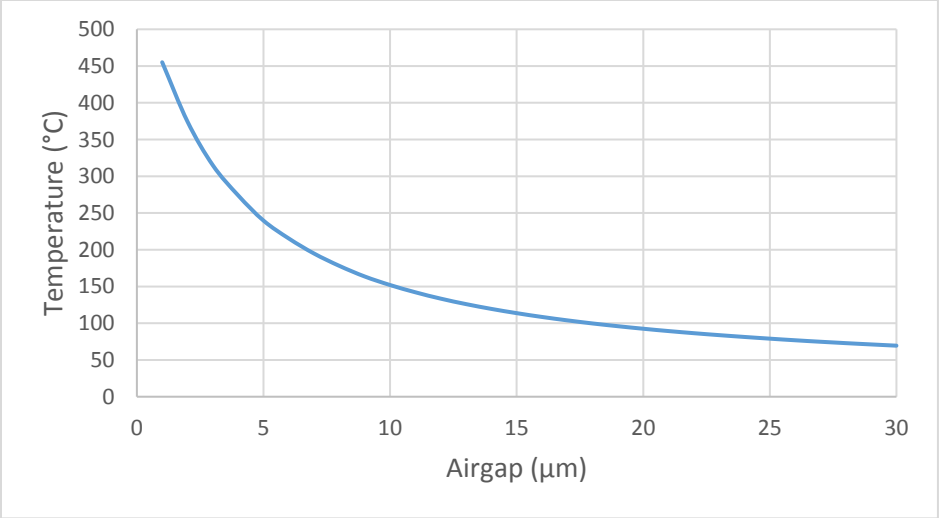

Figure 7 - Temperature on the surface of particles at 10ms

The temperature on the surface of the silver nanoparticles quickly drops off with increases in the air gap. This suggests that it is critical to maintain a small air gap for the process to be successful. For the remainder of this paper, a 2µm air gap will be used.

4.3. Requirements for sintering

Per NovaCentrix (a supplier of silver nanoparticle ink), it is required to sinter silver nanoparticles with a particle size of 50nm at 250°C for 10 minutes [35]. To achieve our objective of millisecond sintering, the sintering temperature needs to be significantly higher. Peng et al has achieved sintering of silver nanoparticles in 1ms using SLS which was found to be at 440°C [36]. In this simulation, we have achieved a temperature of 440°C in 12ms as shown in Figure 8. Although sintering may be achieved before this time, we have shown that our system can achieve a temperature deemed necessary for millisecond scale sintering by previous works.

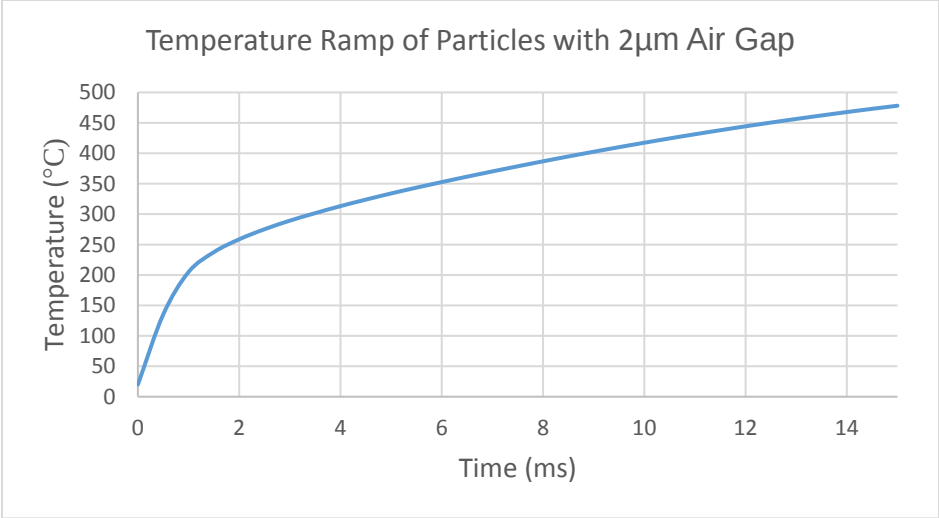

Figure 8 - Maximum temperature experienced at the surface of the particles

4.4. Printing Resolution

Another parameter to determine was the printing resolution. This was evaluated by observing the temperature distribution on the surface of the nanoparticles. The temperature was sampled every 5µm on the surface of silver nanoparticles along the centerline of the microheater as illustrated in Figure 9 by the dotted line, and extending 50µm outside the heater.

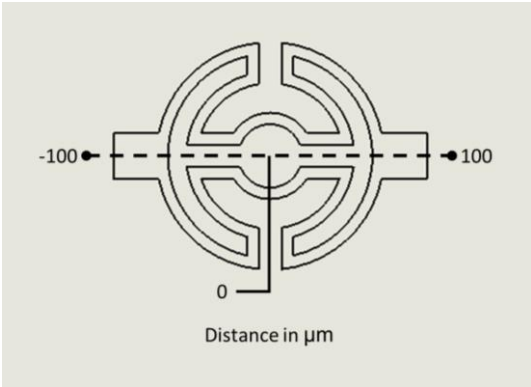

Figure 9 - Line sampled for temperature plot to show resolution

It is observed that there is a sharp decline in the temperature beyond 50µm in either direction from the center of the microheater. The dwell time can be changed to increase or decrease the temperature over this area. The dwell time could be adjusted to accommodate another material with a different required sintering temperature or to achieve a different printing resolution; this is illustrated in Figure 10. It was established previously that a temperature of 440°C is needed for fast sintering of the silver nanoparticles, so in our case a 100µm resolution can be achieved by setting the dwell time to be 14ms.

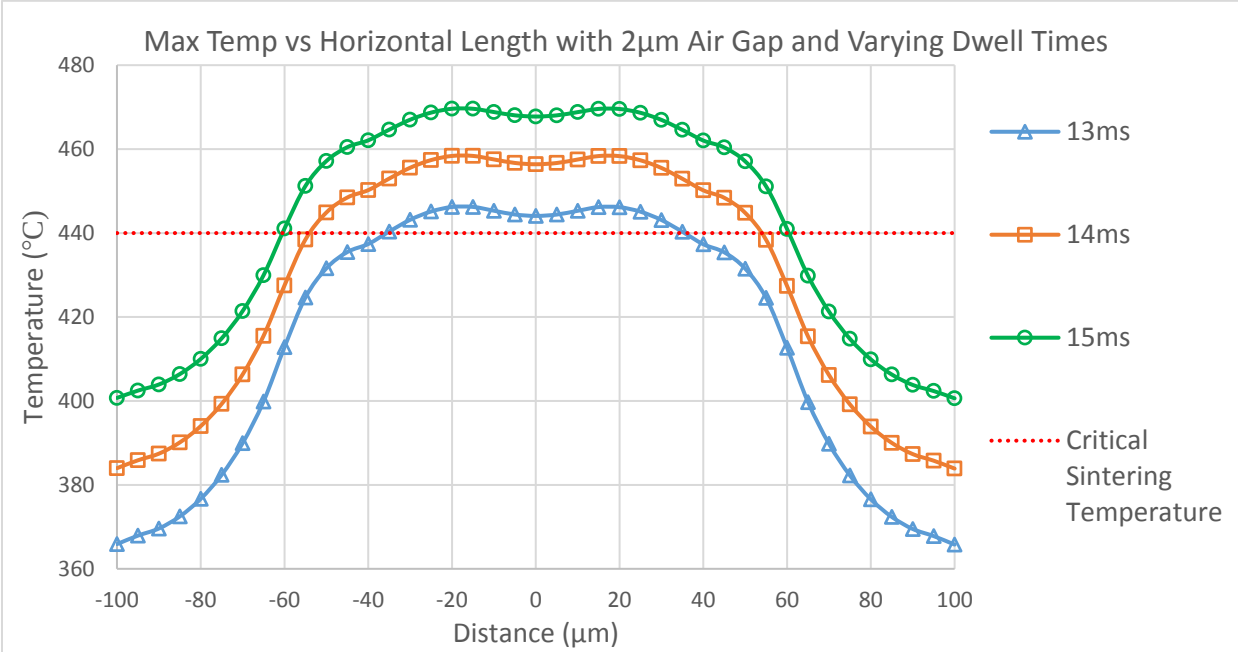

Figure 10 - Temperature along the material underneath the microheater to show resolution. The horizontal line represents a critical sintering temperature of 440°C above which the powder will be sintered. For dwell times of 13, 14, and 15ms, a resolution of 70, 100, and 120µm is achieved respectively.

5. Improvements to Operation

5.1. Optimization of heat flux

The key to improving the MAPS process is to maximize the heat flux into the particles and minimize the heat flux out of the particles. Heat flux is determined by thermal conductivity and temperature gradient as shown in the Equation 3:

$$q_s = -\frac{k\partial T}{\partial x} \tag{3}$$

In this equation q_s is the heat flux out of the surface of the particles. Therefore, to minimize the heat flux out of the particles, the objective is to reduce the thermal conductivity of the printing substrate and to minimize the temperature gradient $\partial T/\partial x$ between the surface of the printing substrate and the particles to be sintered. On the other hand, to maximize the heat flux into the powder particles, the thermal conductivity of the medium (currently air) needs to be increased and the temperature gradient between the heater and the particles to be sintered needs to be maximized.

To numerically prove these concepts, four different cases were set up to illustrate the effects of different material choices on the thermal operation of the system. These cases are as follows (note that case 2 is the same as previously described):

Table 3 - Different cases to be analyzed for their effect on sintering temperature (air gap 2µm)

Case	Substrate	Medium	Initial Powder Bed Temperature (°C)	Purpose

1	Silicon	Air	20	Benchmark
2	Glass	Air	20	Reduce heat flux out of particles (same as before)
3	Glass	Helium	20	Increase heat flux into particles
4	Glass	Helium	100	Heat system before sintering

Each case reveals that when these three parameters are changed, this can have a significant impact on the operation of the system. Figure 11 shows that the heat flux reaches a maximum near 1ms, which is when the heater reaches its operating temperature. Cases three and four achieve a higher net heat flux due to a low thermal conductivity of the glass substrate and a high thermal conductivity of helium.

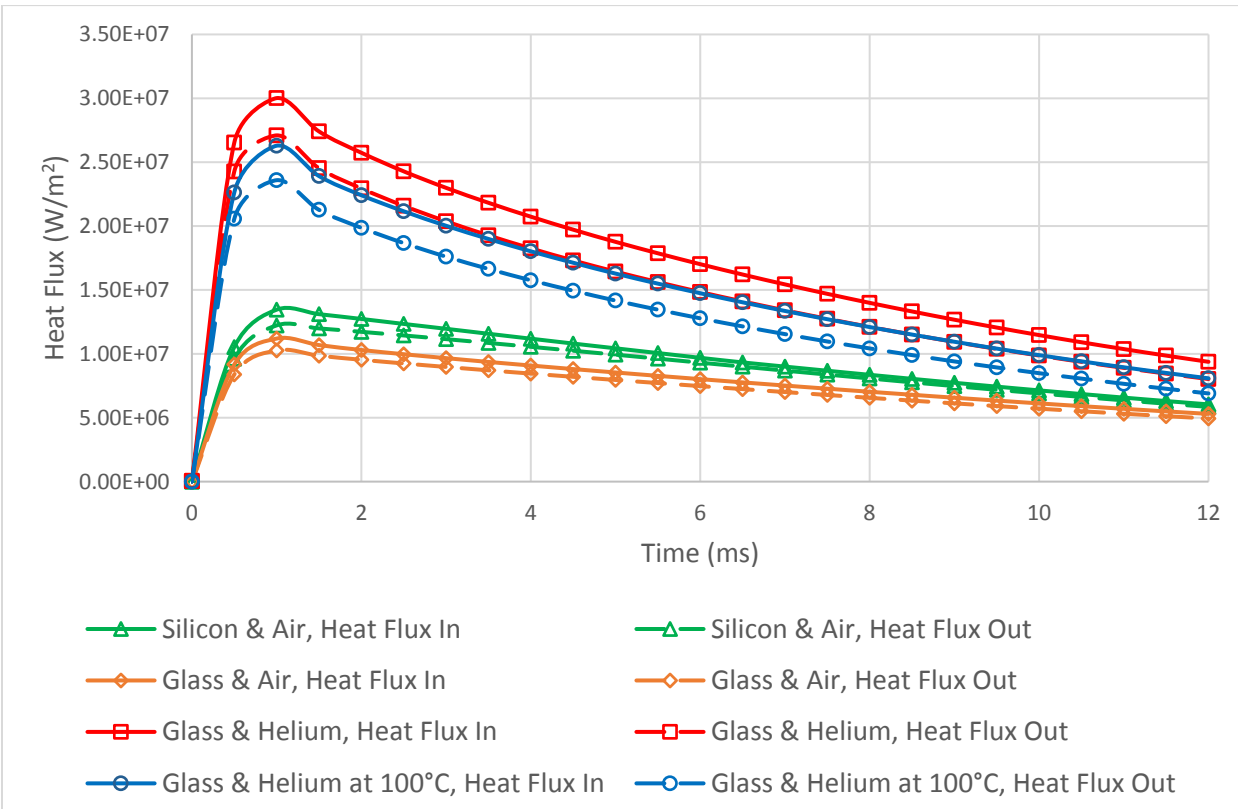

Figure 11 - Heat flux profiles for each case in Table 3

It is important to realize that heat will be added to this system when the heat flux into the particles is greater than the heat flux out of the particles, and a larger difference between these two is most desired; Figure 12 illustrates this relationship. It is seen that case 1 is very ineffective at adding heat to the particles when compared to the other cases due to the high thermal conductivity of a silicon substrate when compared to glass.

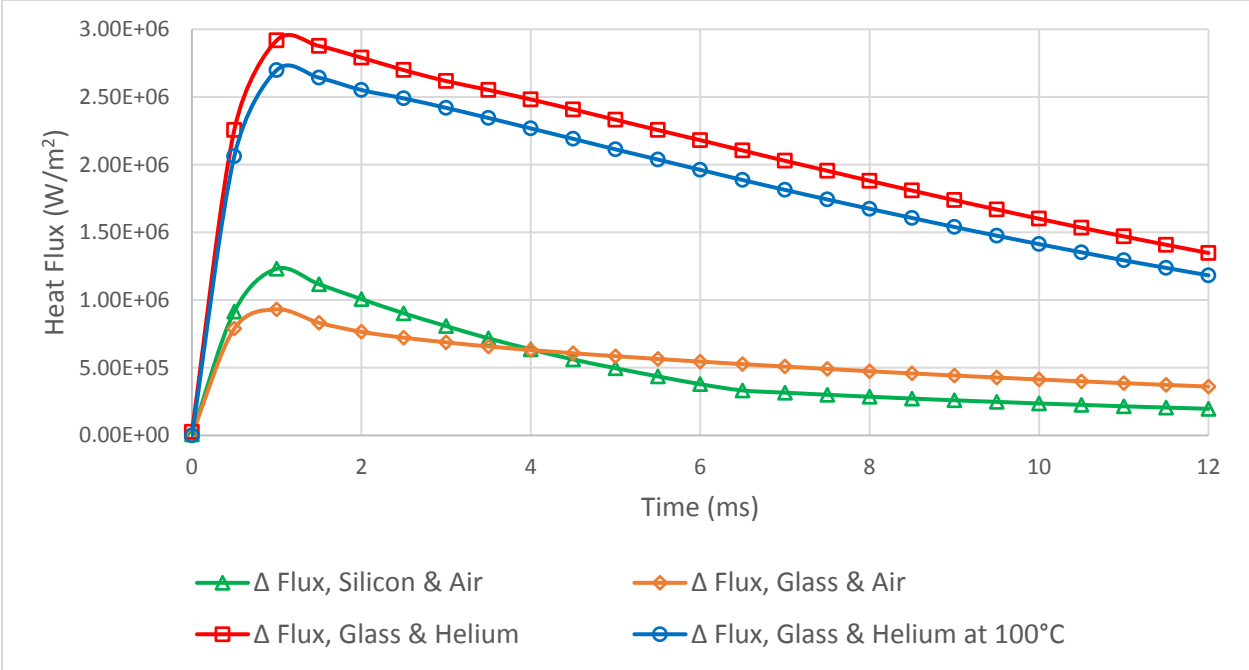

Figure 12 - Heat flux differentials for each case in Table 3

The practical application of this information is to find the amount of time required to reach an acceptable temperature for sintering. It has already been established that a temperature of at least 440°C is required to sinter a silver nanoparticle ink on a millisecond time scale. Figure 13 shows the temperature ramp of the particle layer for each of the four cases. Maximizing the heat flux differential greatly reduces the time required to reach the sintering temperature: case 4 requires only 1.0ms and case 3 requires 1.2ms; both are a vast improvement over the 12ms time required for case 2, which was studied initially.

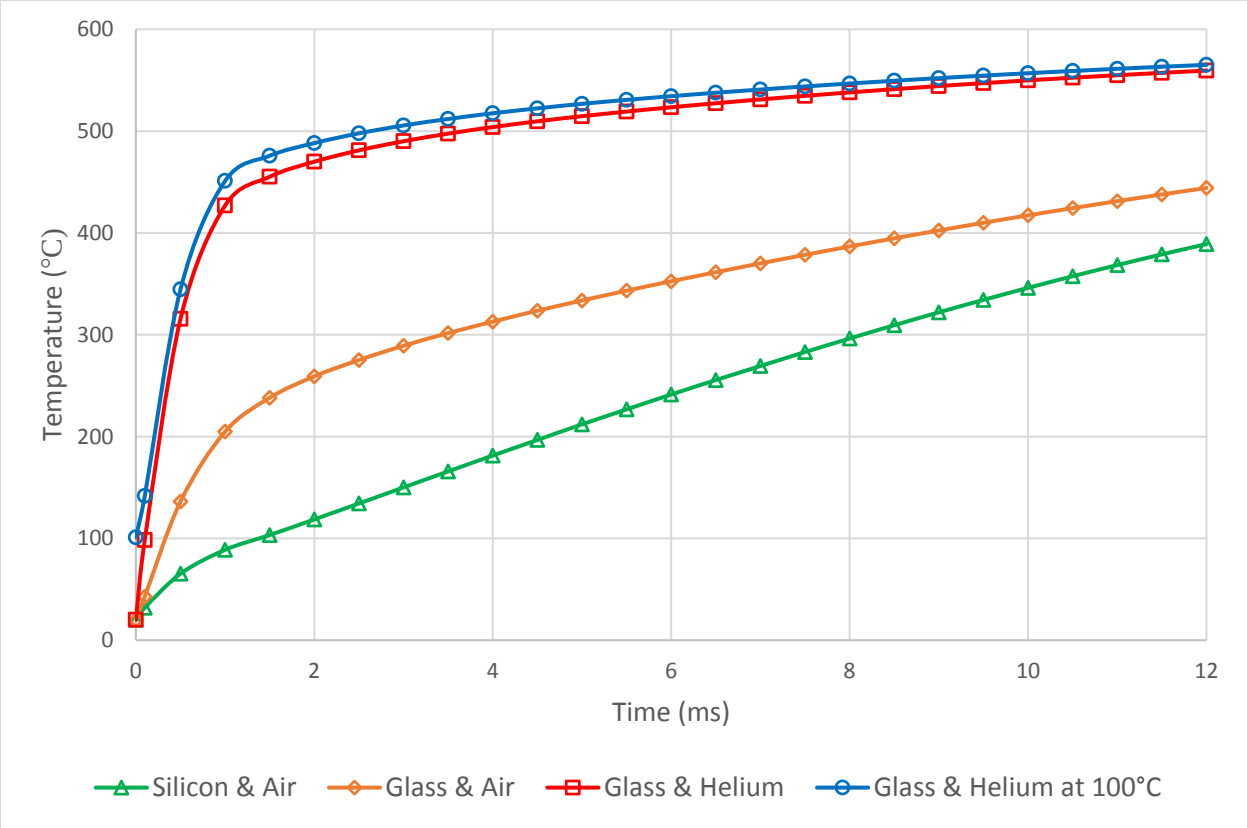

Figure 13 - Temperature ramp of particles for each case in Table 3

It is demonstrated that the MAPS process can be improved with a larger thermal conductivity of the medium gas, a smaller thermal conductivity of the printing substrate, or a smaller air gap. To improve the MAPS process, a combination of these three variables could be changed; for instance, to allow a larger air gap, helium could be used as the conducting medium instead of air. Likewise, the air gap could be minimized and a conducting medium of helium could be used to decrease the time required for sintering, thus allowing a faster operation.

5.2. Comparison to current technologies

The first market that we believe this technology can excel in is the printed electronics market. The current technology uses inkjet or screen printing (a non-digital method) to print a circuit, which then needs to be sintered at a high temperature to achieve high electrical conductivity without damaging the plastic substrate. A pulse lamp is often used to sinter the printed circuits without damaging the plastic substrate [34]. The MAPS technology will provide a digital version of screen printing without any post-processing or damaging the plastic substrate since the heating cycle is very short and the temperature of the plastic substrate won't increase much.

The next application for this technology will be to print 3D parts with plastics and low-melting point metals. The MAPS system was compared to a commercially-available low-cost Prodways SLS printer, which prints nylon. It was found that MAPS consumes 14 times less power, has a greater operation temperature and a much finer resolution [37].

Table 4 - Comparing charactersistics of two types of printers to sinter silver nanoparticles

Brand	Model	Type	Power	Max Temp	Scan Size
ProdWays	P1000	SLS	30W	200C	450µm
-	-	MAPS (New Method)	2.1W	440C	100µm

In addition, the MAPS printer is a scalable printer. The process can theoretically use many microheaters in an array. This can significantly increase speeds and digitalize the printing process. Figure 14 illustrates how a large array of heaters can be used to sinter multiple areas of a powder bed at once. SLS systems can accomplish the same feat by using multiple lasers, but additional lasers add great complexity and expense to the system whereas the microheater array can be scaled at minimum additional cost. Furthermore, the microheaters may provide in-situ monitoring by measuring the resistance of the heater as mentioned earlier.

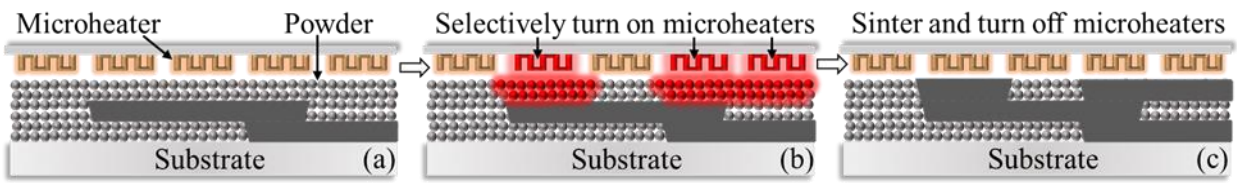

Figure 14 - Illustration of the MAPS process selectively applying localized heat to sinter powder particles using a microheater array

6. Experimental Proof of Concept

Based on the numerical evaluations of the MAPS process, we will provide a preliminary experimental proof of concept in this section. The goal was to demonstrate that a heat pattern could be delivered onto a substrate using the microheater described in this paper. To avoid complications, powders were not used and instead a thermal paper was used to indicate the heat pattern.

6.1. Description of microheater

A microheater array was fabricated using the microheater design for our tests. The microheater was scaled into a 2 x 2 array and the leads were stretched to the edges of the heater die, which measures 7mm x 3.5mm. The heater filaments are made from evaporated titanium and the leads from evaporated gold. A PCB (printed circuit board) package was designed for this experiment. The microheater die was attached to the packaging using epoxy. The electrical connections are made via wire bonding of 5 mils diameter aluminum wires. This packaging is attached to a printhead described in the following section. The fabricated and packaged microheater array is shown in Figure 15. The details of the fabrication, packaging, and feedback control of the microheater array will be presented in a separate paper.

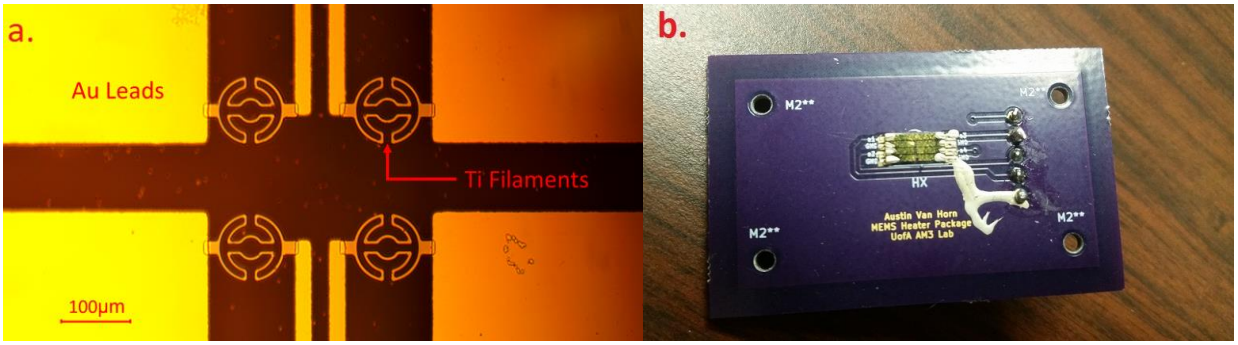

Figure 15 - a. Fabricated microheater array; b. Packaged microheater array

6.2. Description of test sample

To prove that our system can pattern a substrate over an air gap, a thermal paper was used to visualize the heat pattern. Thermal paper is used to print receipts, and turns black when exposed to heat. The thermal paper used in our experiments turns black at a temperature of 70°C. A thin strip of thermal paper was cut and attached to a matching strip of silicon using double sided tape as shown in Figure 16.


Figure 16 - Thermal paper used for experiment attached to a thin silicon strip

6.3. Experimental setup

As indicated in sections 4 and 5, it is critical to maintain a small air gap (a few microns) for this process to work. In this section, we designed a low-cost experimental setup to achieve this objective for the experimental tests.

6.3.1. Design

The following specifications were laid out in the design of the printing stage:

1. A micron scale gap between the printhead and the substrate must be accomplished;
2. The gap distance must be adjustable with sub-micron precision;

3. The printhead and the substrate must maintain the air gap with a variation of less than 1μm throughout the travel of the substrate.

Our general approach is to first achieve a full contact between the printhead and the printing substrate to ensure parallelism between the printhead and the printing substrate and then move the printhead up by the desired air gap. Four key elements to satisfy these design requirements are listed below:

D1. A floating substrate whose height can be adjusted at four corners with submicron precision to make sure that the substrate can achieve full contact with the bottom plane of the printhead;
D2. A mechanism to adjust the height of the entire printhead vertically (i.e., perpendicular to the substrate plane) at submicron precision;
D3. A mechanism to detect contact between the bottom plane of the printhead and the substrate plane at the location of the heater.
D4. The printhead plane and the substrate plane for detecting contact must be near flat, with a sub-micron tolerance across the length of its surface.

With these design elements in mind, we will first adjust the height of the floating substrate (D1) in reference to the bottom plane of the printhead to make sure the substrate and printhead are parallel. Then, the printhead is lowered (D2) until the microheater makes contact with the silicon strip, at which point an LED lights up to signal contact is made (D3). After this zero point is found, the printhead is raised to the desired air gap. The design which accomplishes these goals is described in the following sections.

6.3.2. Assembly

To accomplish the three design goals from the previous section, the following experimental setup was developed. A large base was designed which combines a floating stage and a printhead. A floating stage sits inside of the construct; this stage is supported by four adjustable sub-micron precision screws to satisfy D1. A printhead is suspended over the stage; this printhead incorporates a micrometer which allows the heater to be moved vertically with sub-micron precision to satisfy D2. The microheater is used as a contact sensor to accomplish D3, and D4 is accomplished by using glass slides for horizontal motion. These parts of the assembly are discussed in detail in the following sections.

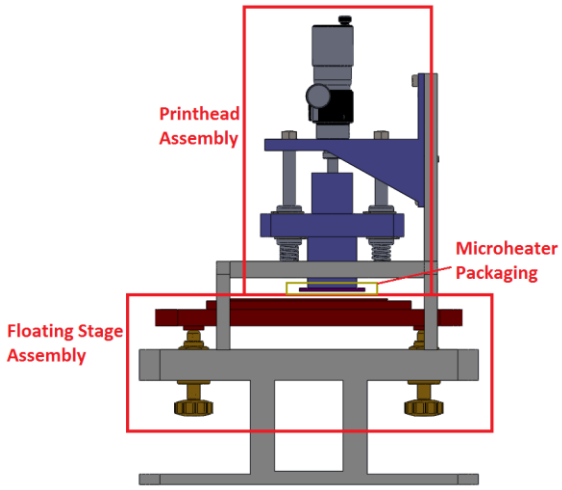

Figure 17 - Section view of the experimental assembly

6.3.2.1. Floating Stage

Four precision adjustment screws support the adjustable base at each of its corners. These are used for fine-adjustment of the height of the floating substrate at four corners to achieve parallelism with the printhead. A glass slide is used as the printing substrate: this will sit on top of a captive slide which is positioned on top of the adjustable stage. The substrate is moved by simply pushing it using a fine tool such as a small screwdriver (which can be automated in the future).

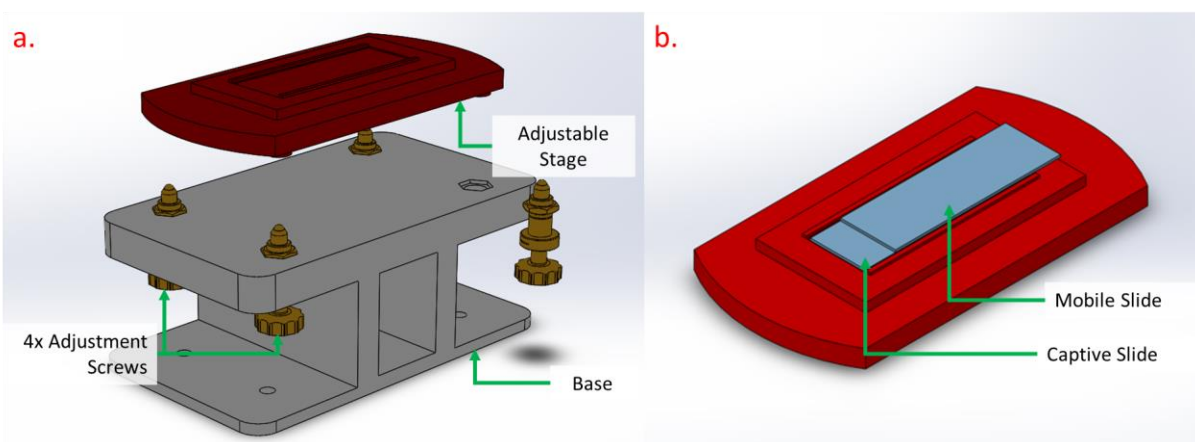

Figure 18 - a. Exploded view of the base and adjustable stage; b. Illustration of slide travel on the adjustable stage

The glass slides were chosen to facilitate horizontal motion of the substrate because the surface of the glass is very smooth (~10s nanometer surface roughness) and flat; this prevented any vertical motion during the travel of the substrate. A microgauge was used to verify this; testing showed that there was no change in elevation more than 1µm throughout the travel of the glass slide as shown in Figure 19.

Figure 19 - Experimental setup to observe the elevation change of the slide as it travels horizontally

6.3.2.2. Printhead Assembly

The printhead assembly consists of two 3D printed frames joined together with linear motion shafts. The microheater packaging is attached to the bottom frame. A micrometer is attached to the top frame and presses against the bottom segment to adjust the height of the microheater. The micrometer has a resolution of 0.5µm and has a lock, and is sufficient to establish the sub-micron gap that we require. Springs keep the printhead system in balance, and also provide the force needed to raise the microheater whenever the micrometer is disengaged.

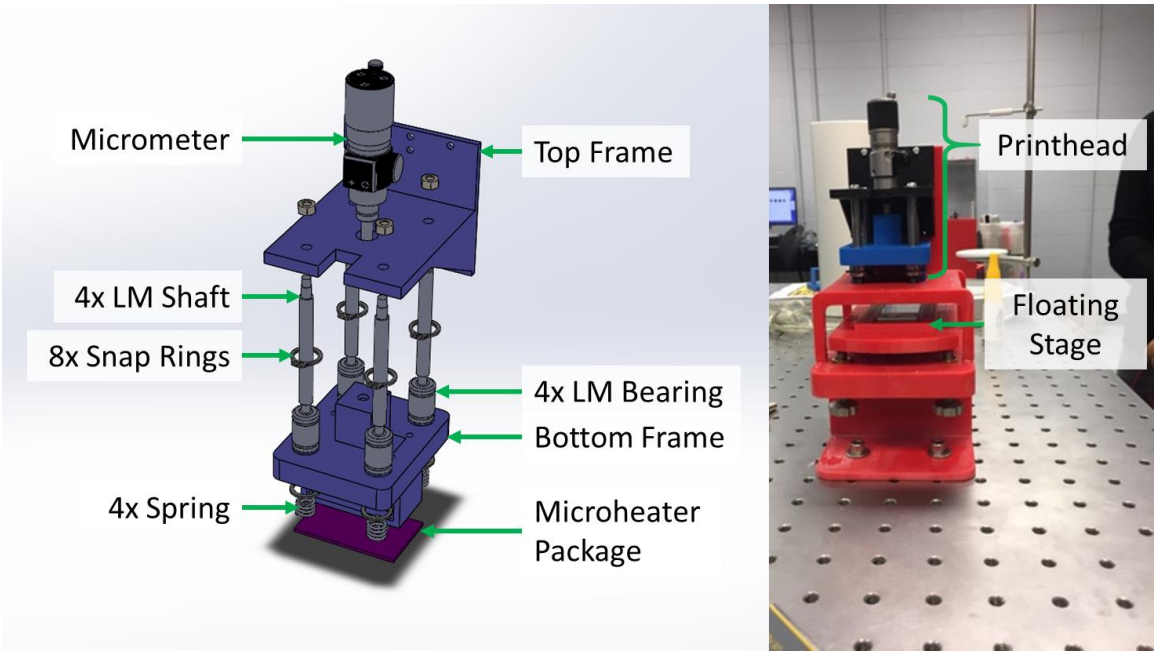

Figure 20 - Exploded view of the printhead; final assembled design

6.3.2.3. Contact Sensor

A thin strip of silicon 0.5mm thick was placed on top of the glass slides of the adjustable stage and used as a substrate in this experiment. The strip of silicon had titanium 100nm thick evaporated on the surface, and the microheater was used as a contact sensor as seen in Figure 21: two of the heaters in the array were connected to a circuit with an LED, so that when the titanium pad met the leads of these heaters, the LED would light up. After contact is achieved, the micrometer can be backed off to produce the desired air gap between the heater and the printing substrate.

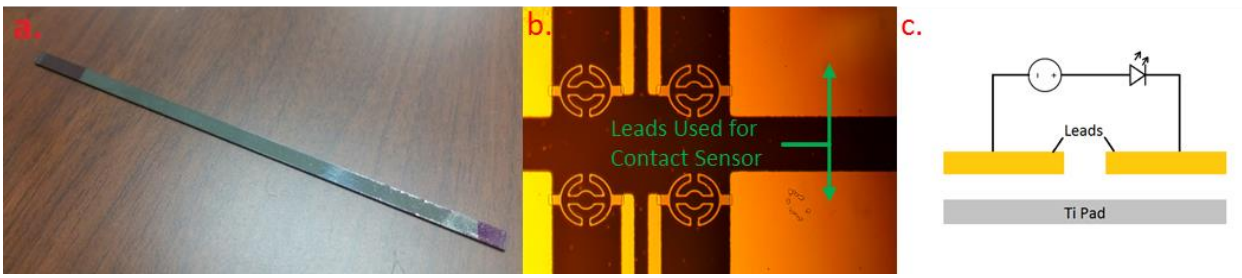

Figure 21 - a. Silicon strip with titanium contact pad used as substrate; b. Leads used for the contact sensor; c. Depiction of circuit for contact sensor - the contact between the leads and the pad act as a switch to light the LED

This entire setup is mostly 3D printed and costs around $300. It is worth noting that this setup can be automated to achieve higher precision at relatively low cost by replacing the precision screws and micrometer with a precision motion stage and several piezoelectric transducers, where the precision motion stage will be used for rough adjustment and piezoelectric transducers used for nanoscale adjustment.

6.3.3. Operation of the experimental setup

The final design was used in proof of concept testing to verify that the microheater was capable of heat transfer to a substrate material. Thermal paper was chosen as a “sintering” material for visualizing the heat pattern, since the paper will turn black upon heating to show the delivered heat pattern. A standard operating procedure was implemented for returning reliable results in subsequent tests. That standard operating procedure is as follows:

1. Adjust the floating stage using the adjustable screws at each corner to be level with the microheater die.
2. Place the silicon strip with titanium pad underneath the microheater.
3. Lower the microheater until contact is made. An LED will indicate contact as mentioned previously.
4. Raise the microheater to allow clearance, record the distance traveled.
5. Remove the silicon strip with titanium pad and replace it with the silicon strip with thermal paper.
6. Accounting for the thickness of the new substrate, lower the microheater to achieve the desired air gap.
7. Apply 55mW power to the heater.
8. Slowly move the silicon strip horizontally underneath the heater, about 5mm per second.
9. After the heater has been moved far enough, turn off the power to the microheater.
10. Raise the microheater to allow clearance and remove the silicon strip.

6.4. Results

By following the above instructions, several marks were made on the thermal paper during multiple experiments, as seen in Figure 22. These marks can be seen clearly with the naked eye, despite the size of the heater being only 100µm in diameter.

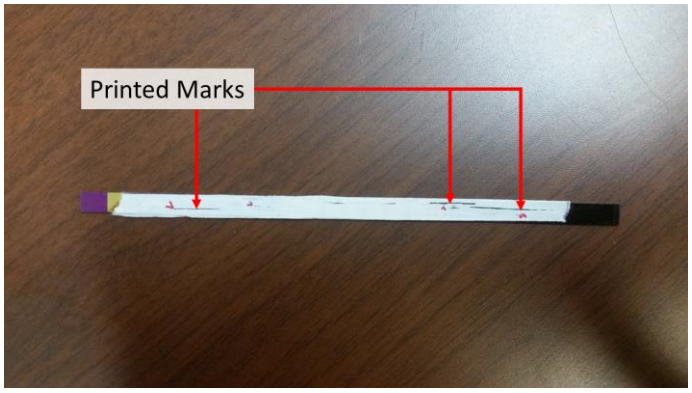

Figure 22 - Marks made on thermal paper using the microheater

Because the thermal paper turns black at a low temperature of only 70°C, the heater was only brought to a temperature of 300°C which was sufficient to bring the thermal paper to the desired temperature; also, such a tight air gap of 2µm was not necessary due to the low temperature requirement, so the air gap was increased to 5µm to show that the microheater can pattern a substrate even over a larger air gap. The result of the experiment using a 5µm air gap can be seen in Figure 23; the trail left by the heater is nearly 1.5 times wider than the diameter of the microheater.

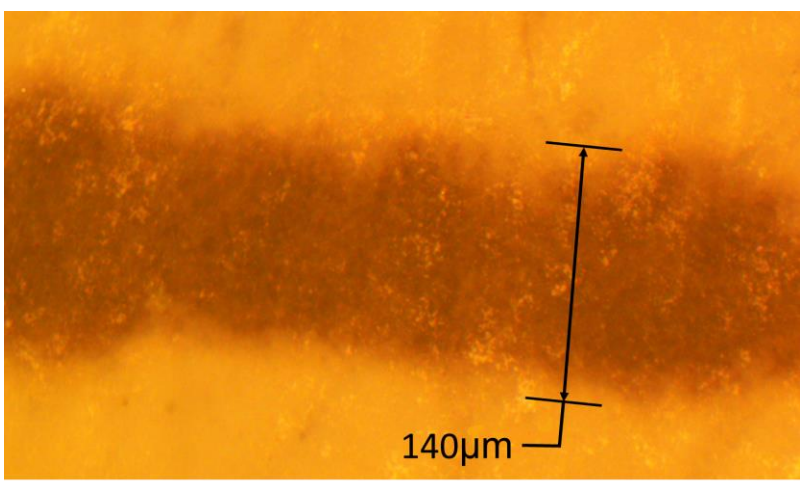

Figure 23 - Mark made by microheater over a 5µm air gap

7. CONCLUSION

In this paper we have presented a novel method of 3D printing via selective resistive sintering. This system could prove to be a viable replacement to selective laser sintering and photonic curing due to the fine resolution, lower power consumption and scalability. We have proposed a design for the microheater and verified it through simulations to show that it can raise the temperature of a printable material over an air gap. Then we have provided a proof of concept by designing a

structure with a printhead and movable substrate which was used to pattern thermal paper. The printer design used in this paper was controlled manually, but the design aspects employed could be used to create one that can be automated. Despite this system being in its infancy, initial testing showed that the microheater designed can be used to print a pattern on thermal material over a small air gap.

7.1. Opportunities for further work

In the future, it will be required that we repeat these tests using other sintering materials, such as silver or nylon particles. To accomplish this, a reliable system of evenly distributing the particles onto a bed must be developed. Further work can be done to improve the heater design to increase its operating temperature to over 1000°C and better power efficiency can be achieved by minimizing heat loss through the substrate of the heater. The temperature profile on the sintering materials can also be changed by improving the design and operation of the microheater to achieve smooth adjustment of printing resolution. The in-situ monitoring capability of this process can be further developed.

8. ACKNOWLEDGEMENTS

We gratefully acknowledge the financial support from the Oak Ridge Associated Universities through the Ralph E. Powe Junior Faculty Enhancement Awards and from the University of Arkansas through the startup fund provided by the Vice Provost Office for Research and Economic Development. We also acknowledge Nick Segovia, Mark Edwards, Kendell Whitehead and Errol Porter for their assistance in developing the experimental proof of concept. Any opinions, findings, and conclusions or recommendations expressed in this publication are those of the authors and do not necessarily reflect the views of the University of Arkansas.

REFERENCES

1. J.J. Beaman and C.R. Deckard, *Selective laser sintering with assisted powder handling*. 1990, Google Patents.
2. M. Agarwala, D. Bourell, J. Beaman, H. Marcus, and J. Barlow, *Direct selective laser sintering of metals.* Rapid Prototyping Journal, 1995. **1**(1): p. 26-36.
3. Y. Kathuria, *Microstructuring by selective laser sintering of metallic powder.* Surface and Coatings Technology, 1999. **116**: p. 643-647.
4. J.-P. Kruth, M.-C. Leu, and T. Nakagawa, *Progress in additive manufacturing and rapid prototyping.* CIRP Annals-Manufacturing Technology, 1998. **47**(2): p. 525-540.
5. J.-P. Kruth, B. Van der Schueren, J. Bonse, and B. Morren, *Basic powder metallurgical aspects in selective metal powder sintering.* CIRP Annals-Manufacturing Technology, 1996. **45**(1): p. 183-186.
6. B. Van der Schueren and J.-P. Kruth, *Powder deposition in selective metal powder sintering.* Rapid Prototyping Journal, 1995. **1**(3): p. 23-31.
7. S. Kumar, *Selective laser sintering: a qualitative and objective approach.* Jom, 2003. **55**(10): p. 43-47.
8. T.R. Mahale, *Electron beam melting of advanced materials and structures*. 2009.
9. I. Gibson, D. Rosen, and B. Stucker, *Additive manufacturing technologies: 3D printing, rapid prototyping, and direct digital manufacturing*. 2014: Springer.
10. M. Khaing, J. Fuh, and L. Lu, *Direct metal laser sintering for rapid tooling: processing and characterisation of EOS parts.* Journal of Materials Processing Technology, 2001. **113**(1): p. 269-272.
11. H. Ho, I. Gibson, and W. Cheung, *Effects of energy density on morphology and properties of selective laser sintered polycarbonate.* Journal of Materials Processing Technology, 1999. **89**: p. 204-210.
12. D. Miller, C. Deckard, and J. Williams, *Variable beam size SLS workstation and enhanced SLS model.* Rapid Prototyping Journal, 1997. **3**(1): p. 4-11.
13. H. Niu and I. Chang, *Selective laser sintering of gas atomized M2 high speed steel powder.* Journal of materials science, 2000. **35**(1): p. 31-38.
14. Y.-A. Song and W. Koenig, *Experimental study of the basic process mechanism for direct selective laser sintering of low-melting metallic powder.* CIRP Annals-Manufacturing Technology, 1997. **46**(1): p. 127-130.
15. R. Patwa, H. Herfurth, J. Chae, and J. Mazumder. *Multi-beam laser additive manufacturing*. in *32nd International Congress on Applications of Lasers and Electro-Optics, ICALEO 2013*. 2013.
16. D.S. Hermann and R. Larson. *Selective Mask Sintering for Rapid Production of Parts, Implemented by Digital Printing of Optical Toner Masks*. in *NIP & Digital Fabrication Conference*. 2008. Society for Imaging Science and Technology.
17. H.R. Thomas, N. Hopkinson, and P. Erasenthiran. *High speed sintering—continuing research into a new rapid manufacturing process*. in *Proceedings of 17th SFF Symposium, Austin, TX*. 2006.
18. B. Khoshnevis, *Selective inhibition of bonding of power particles for layered fabrication of 3-D objects*. 2003, Google Patents.
19. B. Khoshnevis, M. Yoozbashizadeh, and Y. Chen, *Metallic part fabrication using selective inhibition sintering (SIS).* Rapid Prototyping Journal, 2012. **18**(2): p. 144-153.
20. J. Moon, J.E. Grau, V. Knezevic, M.J. Cima, and E.M. Sachs, *Ink- Jet Printing of Binders for Ceramic Components.* Journal of the American Ceramic Society, 2002. **85**(4): p. 755-762.
21. A.S. Basu, S. McNamara, and Y.B. Gianchandani, *Scanning thermal lithography: Maskless, submicron thermochemical patterning of photoresist by ultracompliant probes.* Journal of Vacuum Science & Technology B, 2004. **22**(6): p. 3217-3220.
22. B.C. Chou, *Thermal printing device and methods for manufacturing the same*. 2006, Google Patents.
23. Hartmann, Anders Ørnsholt, and Frederik Walsted Tjellesen. "Three-dimensional printer." U.S. Patent No. 9,421,715. 23 Aug. 2016.
24. C.K. Chua and K.F. Leong, *Rapid prototyping: principles and applications*. Vol. 1. 2003: World Scientific.
25. P. Torabi, M. Petros, and B. Khoshnevis, *Selective inhibition sintering: the process for consumer metal additive manufacturing.* 3D Printing and Additive Manufacturing, 2014. **1**(3): p. 152-155.
26. P. Deng, Y.-K. Lee, and P. Cheng, "*An experimental study of heater size effect on micro bubble generation".* International journal of heat and mass transfer, 2006. 49(15): p. 2535-2544.
27. K. Zhang, S. Chou and S. Ang, "Fabrication, modeling and testing of a thin film Au/Ti microheater," *International Journal of Thermal Sciences*, vol. 46, pp. 580-588, 2007.
28. VanHorn, Austin, and Wenchao Zhou. "Design and optimization of a high temperature microheater for inkjet deposition." The International Journal of Advanced Manufacturing Technology (2016): 1-11.
29. S. Chol, "Enhancing thermal conductivity of fluids with nanoparticles," *ASME-Publications-Fed*, vol. 231, pp. 99-106, 1995.
30. "50 nm Silver Nanospheres," nanoComposix, 2017. [Online]. Available: http://nanocomposix.com/collections/dried-silver/products/50-nm-silver-nanospheres. [Accessed 9 February 2017].

31. L. Ma, J. Fong, B. Lane, S. Moylan, J. Filliben, A. Heckert and L. Levine, "Using design of experiments in finite element modeling to identify critical variables for laser powder bed fusion," in International Solid Freeform Fabrication Symposium, 2015.
32. P. Zehner and E. U. Schlünder, "Die effektive Wärmeleitfähigkeit durchströmter Kugelschüttungen bei mäßigen und hohen Temperaturen," Chemie Ingenieur Technik, vol. 45, pp. 272-276, 1973.
33. S. S. Sib, J. W. Barlow and T. Austin, "MEASUREMENT AND PREDICTION OF THE THERMAL CONDUCTIVITY OF POWDERS ATIDOHTEMPERATURES," .
34. M. J. Guillot, S. C. McCool and K. A. Schroder, "Simulating the thermal response of thin films during photonic curing," in *ASME 2012 International Mechanical Engineering Congress and Exposition*, 2012, pp. 19-27.
35. *Metalon® JS-B40G*, NovaCentrix, 2015
36. P. Peng, A. Hu, Y. Zhou, *Laser sintering of silver nanoparticle thin films: microstructure and optical properties*. Applied Physics A, 2012. **108**(3).
37. ProMaker P1000 Preliminary Specifiications. Available: http://www.prodways.com/en/printer/promaker-p1000/.